Applied Surface Science 580 (2022) 152237

Contents lists available at ScienceDirect

Applied Surface Science

journal homepage: www.elsevier.com/locate/apsusc

Full Length Article

Surface engineered polar CeO_2-based cathode host materials for immobilizing lithium polysulfides in High-performance Li-S batteries

Zhen Wei, Junhao Li, Ruigang Wang *

Department of Metallurgical and Materials Engineering, The University of Alabama, Tuscaloosa, AL 35487, United States

ARTICLE INFO

Keywords:
Li-S battery
Shuttle effect
CeO_2 nanocrystals
Shape-controlled synthesis
Host materials

ABSTRACT

The particle morphology of CeO_2 nanocrystals with different exposed crystal facets is a crucial factor influencing the surface-related materials performance. In this report, shape-controlled synthesis of CeO_2 nanocrystals with various preferentially exposed crystal facets (CeO_2 nanorods with (110)/(100)/(111), CeO_2 nanocubes with (100) and CeO_2 nanoctahedra with (111)) was conducted aiming to investigate the crystal plane effect of polar CeO_2 as a cathode host on the immobilization of lithium polysulfides and electrochemical performance of the assembled Li-S batteries. The strong chemical bonding between lithium polysulfides and CeO_2 host, including Ce-S and Li-O bonds formed on the exposed (110)/(100) and defected (111) crystal facets of CeO_2 nanorods during reversible electrochemical conversion from soluble long-chain polysulfides to insoluble short-chain Li_2S/Li_2S_2, results in superb diffusion restriction of lithium polysulfides towards Li anode and endows CeO_2 nanorods@CC electrode with a superior electrochemical property among three tested electrodes of CeO_2 nanorods@carbon cloth (CC), CeO_2 nanocubes@CC, and CeO_2 nanoctahedra@CC. However, such strong chemical interaction against polysulfides was not observed by CeO_2 nanocubes with preferentially exposed (100) crystal planes and CeO_2 nanoctahedra with preferentially exposed (111) crystal planes. In addition to the factor of the exposed crystal planes, CeO_2 nanorods possess defect-rich surfaces (i.e., oxygen vacancies and Ce^{3+}) also serving as possible polysulfides anchoring sites, which can contribute to effective immobilization of lithium polysulfides. Benefiting from the above-mentioned advantages, CeO_2 nanorods are considered as an outstanding candidate of cathode host materials for long life and high-performance Li-S batteries.

1. Introduction

To effectively address the parasitic issues of highly polluted environment due to burning conventional fossil fuels, novel environmentally friendly and sustainable energy production and storage systems are urgently needed, i.e., replacing fossil fuels driven vehicles by electric vehicles. Rechargeable lithium-ion batteries (LIBs) have been extensively investigated and utilized over the past two decades since their commercial launch in the early 1990s by Sony. However, conventional LIBs have already reached their theoretical energy density (150–200 Wh kg^{-1}), so they are difficult to meet the continuously rising demands in fast-developing portable electronics, advanced electric vehicles and grid storage for intermittent renewable energy storage from solar and wind resources [1]. There is an urgent demand to develop rechargeable energy storage systems with excellent attributes such as low-cost fabrication, fast charging, great cyclability and high energy density. Lithium sulfur batteries (LSBs), considered as one of the most favorable candidates to meet the above-mentioned requirements, have attracted ever-increasing attention due to their remarkably high theoretical capacity of 1675 mAh g^{-1}, high theoretical energy density of 2600 Wh kg^{-1} and low cost of sulfur ($40 per metric ton in 2020) [2–5]. Despite many favorable advantages of elemental sulfur cathode including non-toxicity, natural abundance and low cost, the practical large-scale commercialization of rechargeable LSBs is restricted by several intractable technical challenges, including (1) poor electronic conductivity of sublimed sulfur and lithium sulfide (Li_2S: discharge product) [6,7]; (2) formidable volumetric expansion of sulfur (~80%) during charge–discharge cycling process [6,7]; (3) highly soluble long-chain intermediate polysulfide species can easily dissolve into organic solvents upon the formation and huge loss of active materials is caused by the diffusion of a significant amount of dissolved intermediate polysulfide species from the cathode side to the lithium metal anode side, which is known as “shuttle effect” [6–11]. The combination of these technical challenges leads to fast capacity decay, low sulfur utilization and cycling

* Corresponding author.
E-mail address: rwang@eng.ua.edu (R. Wang).

https://doi.org/10.1016/j.apsusc.2021.152237
Received 30 October 2021; Received in revised form 8 December 2021; Accepted 14 December 2021
Available online 17 December 2021

instability of LSBs.

In order to mitigate those aforementioned technical limitations of LSBs, enormous efforts have been devoted to formulating and assessing the feasibility of a number of trapping strategies of lithium polysulfides. Firstly, incorporating insulating sublimed sulfur with highly conductive carbonaceous nanomaterials to fabricate multifunctional hybrid composites has been enormously successful in the field of LSBs, due to their remarkable physical confining capability against polysulfides and excellent electronic conductivity of carbon materials in various forms. Therefore, diverse high-surface-area carbonaceous host nanomaterials with various dimensionalities, sizes and morphologies were innovatively developed, including 0D microporous/mesoporous carbon particles [12], 1D carbon nanomaterials like multi-walled carbon nanotubes (MWCNT) [13] and 2D nanostructured layered carbon materials like graphene [14]. However, for long-term electrochemical cycling, limited restriction of polysulfide diffusion was achieved using the aforementioned diverse carbonaceous host nanomaterials due to their non-polar nature leading to weak affinity against lithium polysulfides species. Therefore, enormous attention has been paid to numerous metal sulfides, metal nitrides and metal oxides hosts and/or additives due to their polar-nature surface with strong polysulfides adsorption capability. Particularly, varied metal oxides (ZnO [15], Fe_3O_4 [16], V_2O_3 [17], Ta_2O_5 [18], and MnO [19]) have been reported to successfully entrap polysulfides, resulting in enhanced sulfur utilization and battery cell performance.

Recently, polar CeO_2 has been reported as effective polysulfides absorbent in the cathode of LSBs. For example, Ma et al. [20] reported that their assembled LSBs exhibited high reversible capacity of 1066 mAh g^{-1} at 0.2C after 200 cycles and 836 mAh g^{-1} at 1C after 500 cycles, with an efficient sulfur host material prepared by implanting CeO_2 nanocrystals homogeneously into well-designed bimodal micro- and *meso*-porous nitrogen-rich carbon nanospheres. Later Qi et al. [21] designed a hollow nanosphere structure with CeO_2/ultrathin nitrogen-doped carbon shells as sulfur host for LSBs, which demonstrated a high reversible capacity of 1348 mAh g^{-1} at 0.2C and superior cycle stability (632 and 458 mAh g^{-1} at 2C and 5C after 500 cycles, respectively). In another study, Xiao et al. [22] also achieved good specific capacities of 1359 and 715 mAh g^{-1} at rates of 0.1C and 1C, respectively, using CeO_2-webbed carbon nanotubes (CeO_2@CNT) as sulfur absorbent for LSBs.

Meanwhile, the investigation of diverse CeO_2 nanocrystals with different morphologies including nanorods, nanocubes and nanoctahedra has been extensively conducted in the field of catalysis for various gas or chemical conversion applications such as ethanol reforming [23], CO oxidation [24], H_2 oxidation [25], catalytic ozonation [26], H_2S selective oxidation [27], dimethyl carbonate synthesis [28], 2-chloroethylethyl sulfide degradation [29], HCl oxidation [30], and NO reduction [31] due to the crystal plane-dependent materials properties. Different nanoshaped CeO_2 has their own preferentially exposed crystal facets (thermodynamically stable or metastable), which is a significant determining factor influencing the catalytic activity and selectivity when used in the field of redox related catalysis. Typically, CeO_2 nanorods (CeO_2 NR) preferentially expose (1 1 0) and (1 0 0) or defected (1 1 1) crystal facets, CeO_2 nanoctahedra (CeO_2 NO) are enclosed by dominant (1 1 1) crystal planes and CeO_2 nanocubes (CeO_2 NC) only exhibit (1 0 0) crystal planes [32].

Recently, shaped-controlled synthesis of various metal oxide nanocrystals used in electrodes for diverse rechargeable battery systems such as LSBs [33,34], Na-ion batteries [35] and LIBs [36] has been investigated. It appears that the morphology and surface structure of metal oxide hosts or additives are important factors affecting electrochemical performance of the batteries due to their impact on various intrinsic properties such as surface area, adsorption, and redox related behavior. To the best of our knowledge, a comprehensive investigation on morphology-dependent electrochemical properties of surface-engineered CeO_2 nanocrystals used as sulfur host or additive for rechargeable LSBs has not been conducted. Herein, morphology-controlled synthesis of diverse CeO_2 additives with different preferentially exposed crystal facets (CeO_2 NR with (1 1 0) and (1 0 0) and (1 1 1), CeO_2 NC with (1 0 0), and CeO_2 NO with (1 1 1)) was implemented aiming to understand the role of CeO_2 termination surfaces and surface defects on the electrochemical performance of the assembled LSBs. Hereinafter, the developed electrodes composed of self-supporting carbon cloth (CC) with decorated CeO_2 NR, CeO_2 NO and CeO_2 NC are refereed as CeO_2 NR@CC, CeO_2 NO@CC, and CeO_2 NC@CC respectively.

2. Experimental section

2.1. Preparation of CeO_2 NR@CC, CeO_2 NO@CC and CeO_2 NC@CC

The preparation of CeO_2 NR@CC and CeO_2 NC@CC was completed by an one-step *in situ* hydrothermal deposition method as previously reported [37]. Typically, 8 mL of 6.0 M aqueous NaOH (VWR, 99%) was added into 88 mL of 0.1 M $Ce(NO_3)_3{\cdot}6H_2O$ (Acros Organics, 99.5%) solution and subsequently the mixed solution was stirred vigorously for ~ 15 s. A free-standing carbon cloth (Fuel cell earth, 20 cm × 20 cm, thickness = 0.381 mm, density = 1.75 g/cm^3) was firstly cut into a 3.5 cm × 3.5 cm piece and then placed into a 200 mL Teflon-lined autoclave before the mixed solution was poured into it. The hydrothermal synthesis was conducted in a programmable box furnace at 90 °C and 150 °C with a dwell time of 48 h to obtain CeO_2 NR@CC and CeO_2 NC@CC respectively. After the hydrothermal reaction, the autoclave was cooled down to room temperature, CeO_2 NR@CC and CeO_2 NC@CC were collected and washed thoroughly with DI water to eliminate Na^+ and other residual ions. After rinsing, CeO_2 NR@CC and CeO_2 NC@CC were transferred into a vacuum drying oven and the samples were collected after drying at 60 °C overnight.

The preparation of CeO_2 NO@CC was achieved by a slightly different procedure compared to those of CeO_2 NR@CC and CeO_2 NC@CC. Firstly, CeO_2 NR powder was obtained by the hydrothermal reaction as described above. Subsequently, the CeO_2 NR powder was calcined at 600 °C for 6 h to fulfill a morphological conversion from nanorods to nanoctahedra. After the thermal calcination, CeO_2 NO powder was obtained. CeO_2 NO@CC was prepared by directly drop-casting the suspension solution containing CeO_2 NO powder onto free-standing carbon cloth. Finally, CeO_2 NO@CC was obtained after drying at 60 °C overnight. In this study, the loading content of CeO_2 was measured based on the difference between the mass of bare carbon cloth disc (diameter = 15 mm, ~21 mg) and the mass of loaded CeO_2 NR@CC disc (diameter = 15 mm, ~22 mg). Therefore, the content of CeO_2 in CeO_2 NR@CC can be calculated as: 22 mg-21 mg = 1 mg. The weight percentage of CeO_2 can be determined as:

$$\frac{1\ mg}{22\ mg} \times 100\% = 4.55\%$$

2.2. Preparation of Li_2S_6 solution and polysulfide adsorption test

1.0 M Li_2S_6 solution was prepared by directly adding sublimed elemental sulfur powder (Alfa Aesar, ≥ 99.5%) and Li_2S (Alfa Aesar, ≥ 99.9%) with a molar ratio of 5:1 into a liquid organic electrolyte containing 1.0 M lithium bis(trifluoromethane) sulfonimide (LiTFSI) (AdipoGen Life Sciences, ≥ 99%) and 0.5 M $LiNO_3$ (Alfa Aesar, 99.999%) mixed with dioxolane:dimethoxyethane (DOL:DME) (1:1 by volume ratio) (Alfa Aesar, 99%). To thoroughly dissolve sulfur and Li_2S, the previously obtained mixed suspension solution was heated on a hot plate at 60 °C for 24 h with vigorously stirring inside an Argon-filled glovebox. The final solution had a reddish color without apparent sediment. The chemical reaction involved is shown below:

$$Li_2S + 5S = Li_2S_6$$

Specifically, 0.002 mol (92 mg) of Li_2S and 0.01 mol (320 mg) of sulfur were dissolved into 2 mL blank electrolyte. After thoroughly stirring and heating, the reddish-colored solution containing 412 mg of Li_2S_6 was obtained. Theoretically, 1 μL of the reddish-colored solution contains 0.206 mg of Li_2S_6. It is worth noting that sulfur is the active material and the amount of sulfur involved in 1 μL of the reddish-colored solution can be calculated through the equation below:

$$0.206\ mg\mu L^{-1} \times \frac{6 \times 32\ gmol^{-1}(molar\ mass\ of\ sulfur)}{206\ gmol^{-1}(molar\ mass\ of\ Li_2S_6)} = 0.192\ mg\mu L^{-1}$$

To implement polysulfide adsorption test, 1.0 M polysulfide solution was diluted to 3.0 mM Li_2S_6 solution. 25 mg of CeO_2 NR, CeO_2 NO and CeO_2 NC powders were placed separately into three 2 mL vials of 3.0 mM Li_2S_6 solution. Photos were taken at the beginning of the test and after 1 h of adsorption.

2.3. Cell assembly

The previously obtained CeO_2 NR@CC, CeO_2 NO@CC and CeO_2 NC@CC were punched out into circular disks with 15 mm diameter. By measuring the mass change of the circular disks (diameter = 15 mm) with and without CeO_2 loading, the mass loading of different shaped CeO_2 nanocrystals can be determined. The corresponding mass loading of CeO_2 NR, CeO_2 NO and CeO_2 NC was properly controlled within the range (0.9 ~ 1.1 mg, corresponding to the areal density of 0.51 ~ 0.62 mg cm^{-2}). The circular disks of CeO_2 NR@CC, CeO_2 NO@CC and CeO_2 NC@CC were coated with a slurry prepared by mechanically mixing super P carbon black (Alfa Aesar, ≥ 99%) used as conductive agent and polyvinylidene fluoride (PVDF) used as binder in N-methyl-2-pyrrolidone (NMP) solvent, which was followed by vacuum drying at 60 °C overnight. For each circular disk (diameter = 15 mm), the mass loadings of the super P and PVDF binder were 0.9 and 0.1 mg, respectively. These three different shaped CeO_2 coated CC disks were used as the cathodes in this work. The CR2032 coin-type cell assembly was conducted in an Argon-filled glovebox with the oxygen and moisture levels lower than 0.1 ppm. Lithium metal and Celgard 2400 membrane were used as the anode and separator, respectively. Firstly, 9.2 μL of Li_2S_6 solution was dropped onto the disks (diameter = 15 mm, area = 1.77 cm^2) of CeO_2 NR@CC, CeO_2 NO@CC and CeO_2 NC@CC, fulfilling a sulfur mass loading of 1.77 mg (areal sulfur loading of 1 mg cm^{-2}). Then, 30 μL of the electrolyte (1.0 M LiTFSI and 0.5 M $LiNO_3$ dissolved in mixed DME and DOL solvent with a volume ratio of 1:1) was dropped onto each of the cathode disks. Next, the separator was placed on the top of the cathode disks, which was followed by adding another 30 μL of the electrolyte. Finally, the lithium metal anode was placed on the top of the cathodes.

2.4. Materials characterization

The morphological and structural characterization of the investigated CeO_2 NR@CC, CeO_2 NO@CC and CeO_2 NC@CC was carried out by using scanning electron microscopy (SEM, JEOL 7000 FE) coupled with an Oxford Instruments energy dispersive X-ray spectrometer (EDS). Transmission electron microscopy (TEM, FEI Tecnai F-20) operated at 200 kV was used to obtain the particle size, morphology and atomic level structures of CeO_2 NR, CeO_2 NO and CeO_2 NC. The preparation of TEM samples consists of several simple steps: firstly, ultrasonicating CeO_2 NR, CeO_2 NO and CeO_2 NC powders in ethanol using three 25 mL vials; secondly, dropping homogeneous CeO_2 NR, CeO_2 NO and CeO_2 NC suspension solution onto ultrathin carbon film attached to a 400-mesh copper grid (Ted Pella Inc.); finally, letting CeO_2 NR, CeO_2 NO and CeO_2 NC dispersion dry in a fume hood. The dried CeO_2 NR, CeO_2 NO and CeO_2 NC samples were directly used for TEM analysis. A Kratos Axis Ultra DLD spectrometer equipped with monochromatic Al Kα radiation (hν = 1486.6 eV) under ultra-high vacuum (10^{-10} Torr) was used to perform X-ray photoelectron spectroscopy (XPS) analysis. The carbon peak C 1 s (284.8 eV) was used as a reference to calibrate the binding energy drift due to possible charging issue. CasaXPS software was used to implement the fitting and deconvolution of peak spectra. A Horiba LabRAM HR 800 Raman spectrometer equipped with a spectral window ranging from 100 to 1200 cm^{-1} and a 100 long-working-distance objective (NA = 0.60) was used to collect the Raman spectra. The calibration of Raman spectra was achieved by using a silicon single-crystal wafer as the reference (520.7 cm^{-1}).

2.5. Electrochemical measurement

Galvanostatic charge discharge cycling was implemented on an MTI battery tester within a voltage window ranging from 1.7 V to 2.8 V with various current densities (1C = 1675 mAh g^{-1}). Cyclic voltammetry (CV) measurement within a voltage potential window of 1.7–2.8 V at a scan rate of 0.1 mV s^{-1} was carried out on a Gamry Potentiostat/Galvanostat workstation (Gamry Interface 1000E). Electrochemical impedance spectroscopy (EIS) measurement with a frequency range of 0.01–10^5 Hz was implemented on the same Gamry Instrument. All the electrochemical measurements were conducted at room temperature (20 °C).

3. Results and discussion

3.1. Morphological characterization before cycling

Fig. 1 illustrates the fabrication processes of CeO_2 NR@CC, CeO_2 NO@CC and CeO_2 NC@CC and the detailed procedure is described in the experimental section. **Fig. S1** exhibits the XRD patterns of CeO_2 NR, CeO_2 NC and CeO_2 NO powders. The representative diffraction peaks can be observed at 28.5, 33.1, 47.5, 56.3, 59.1, 69.4, 76.7, 79.1 and 88.4° for all three CeO_2 samples, corresponding to face centered cubic CeO_2 phase with fluorite structure (JCPDS#: 34–0394). The morphological characterization of *in situ* hydrothermally deposited CeO_2 on CC was conducted using scanning electron microscopy (SEM). As demonstrated in **Fig. S2 a-c**, CeO_2 NR synthesized via hydrothermal method were directly attached onto the individual carbon fibers of free-standing carbon cloth that was placed at the bottom of Teflon-lined stainless-steel autoclave prior to hydrothermal reaction. The localized formation of a dense and uniform CeO_2 NR layer was easily observed from the enlarged SEM image (**Fig. S2 c**), showing the strong anchoring effect of CeO_2 NR onto the individual carbon fibers. Similarly, CeO_2 NC were uniformly covered onto the individual carbon fibers forming a dense layer, as exhibited in **Fig. S2 g-i**. In contrast to CeO_2 NR@CC and CeO_2 NC@CC, from **Fig. S2 d-e**, it appears that there is a greater density of particle agglomeration and weak attachment of CeO_2 NO on the carbon fibers. EDS elemental mapping was used to further investigate the CeO_2 distribution on carbon cloth. As displayed in **Fig. S3 a-c**, all three CeO_2 nanocrystals were homogeneously distributed throughout the 3-D interconnected and highly conductive self-supporting carbon cloth framework.

Transmission electron microscopy (TEM) was used to provide the particle size, morphology and atomic level structural information about three different shaped CeO_2. As exhibited in Fig. 2 **a-b**, rod-like morphology can be clearly seen from the TEM images of CeO_2 NR. The exposed (1 1 0) crystal facet was validated by the HRTEM images of CeO_2 NR with an interplanar spacing of 0.19 nm as shown in Fig. 2 **c-d**. The (1 0 0) and (1 1 1) crystal facets of CeO_2 NR were also observed. Fig. 2 **e-f** present the octahedron-like morphology of CeO_2 NO. The (1 1 1) crystal facet was confirmed by the HRTEM images of CeO_2 NO with an interplanar spacing of 0.31 nm as exhibited in Fig. 2 **g-h**. As displayed in Fig. 2 **i-j**, cube-like morphology can be easily seen from the TEM images of CeO_2 NC. The exposed (1 0 0) crystal plane was substantiated by the HRTEM images of CeO_2 NC with an interplanar spacing of 0.27 nm as shown in Fig. 2 **k-l**. It should be pointed out that, due to the

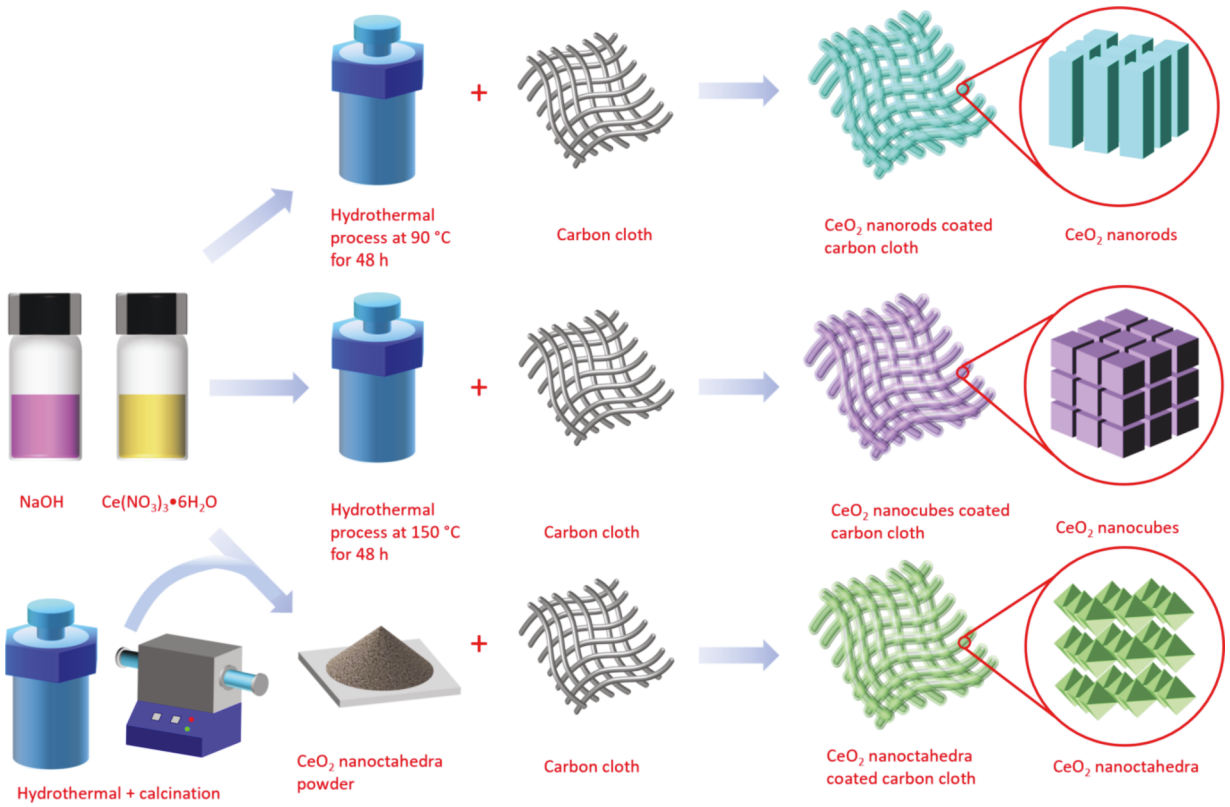

Fig. 1. Schematic diagram showing the preparation routes of CeO_2 NR@CC, CeO_2 NO@CC and CeO_2 NC@CC electrodes.

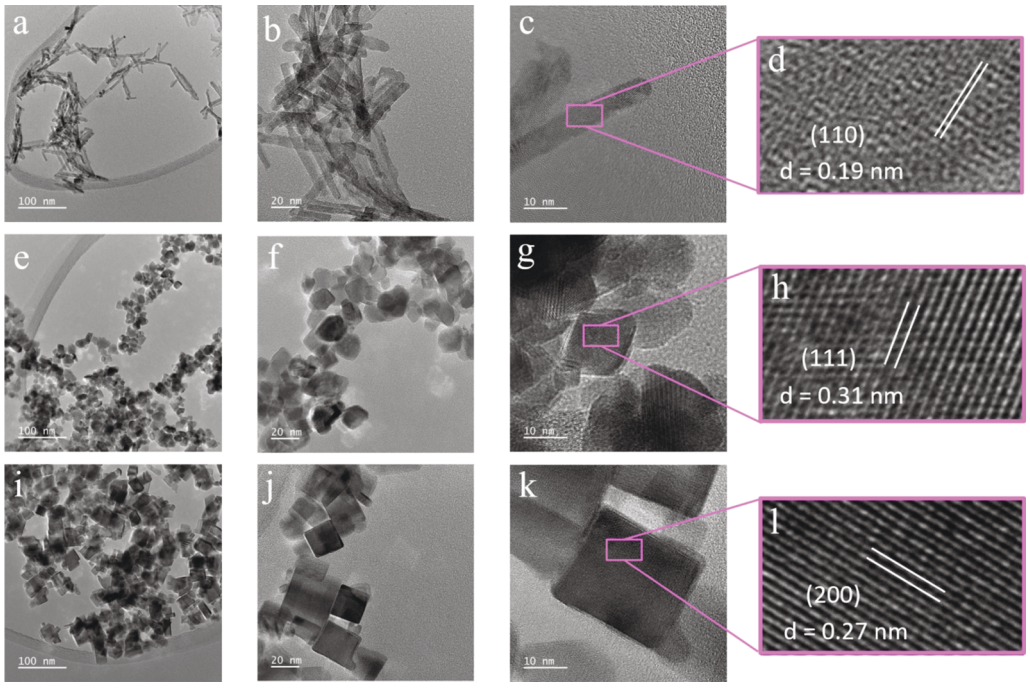

Fig. 2. TEM and HRTEM images of (a-d) CeO_2 NR, (e-h) CeO_2 NO, and (i-l) CeO_2 NC at various magnifications.

difference of SEM/TEM resolution and the sample preparation methods as described in the experimental section, the particle dispersion of CeO_2 is quite different exhibited in the SEM and TEM images (Fig. S2 and Fig. 2).

3.2. Electrochemical characterization

To assess the redox kinetics and the electrochemical performance of three different shaped CeO_2 cathode hosts, CR-2032 button cells were assembled with the same areal sulfur loading of 1.0 mg cm^{-2}. Electrochemical impedance spectroscopy (EIS) with a frequency ranging from

0.01 to 10^5 Hz was carried out to compare the internal impedance and investigate the electrochemical reaction kinetics prior to and after galvanostatic charge discharge cycling test. The equivalent circuit model for the EIS curve analysis is shown in Fig. 3 **a**. The equivalent circuit model consists of the resistance of electrolyte (R_1), the internal phase contact of resistance and its related capacitance in electrode (R_2/CPE_1), the charge-transfer resistance and its related capacitance (R_3/CPE_2), and the CPE for diffusion (CPE_3). As depicted in Fig. 3 **b**, for three fresh coin cells, a semicircle located in the high frequency region can be clearly seen from the EIS curves prior to the galvanostatic cycling, corresponding to the charge transfer resistance (R_{ct}) at the interface between the electrode and liquid organic electrolyte, and an oblique line is situated in the low frequency region related to the Warburg impedance representing the diffusion process of lithium ions in liquid organic electrolyte [38–41]. The diameter of the semicircle of the CeO_2 NR@CC cell is much smaller than those of the CeO_2 NO@CC and CeO_2 NC@CC cells. Quantitatively, the R_{ct} value is 12.44 Ω for the CeO_2 NR@CC electrode compared with the values of 29.98 Ω for the CeO_2 NO@CC electrode and 32.12 Ω for the CeO_2 NC@CC electrode. This low impedance typically leads to accelerated charge transfer enabling favorable improvement of sluggish redox kinetics and facilitated electrochemical transformation of lithium polysulfides for the CeO_2 NR@CC electrode [42]. In comparison, as displayed in Fig. 3 **c**, the EIS plots of three cycled coin cells demonstrated that one small semicircle in the high frequency region is related to the formation of solid Li_2S_2/Li_2S film and one big semicircle in the middle frequency region is associated with the charge transfer resistance [42]. A dramatic decrease in the charge transfer resistance of three different shaped CeO_2 electrodes was clearly observed owing to rearrangement of the active materials and better electrolyte wettability after the initial charge discharge galvanostatic cycles [43]. Among three different electrodes with CeO_2 additives after the galvanostatic cycling process, the CeO_2 NR@CC electrode cell had the lowest charge transfer resistance indicating superior electronic/ionic transport capability and accelerated redox kinetics of intermediate

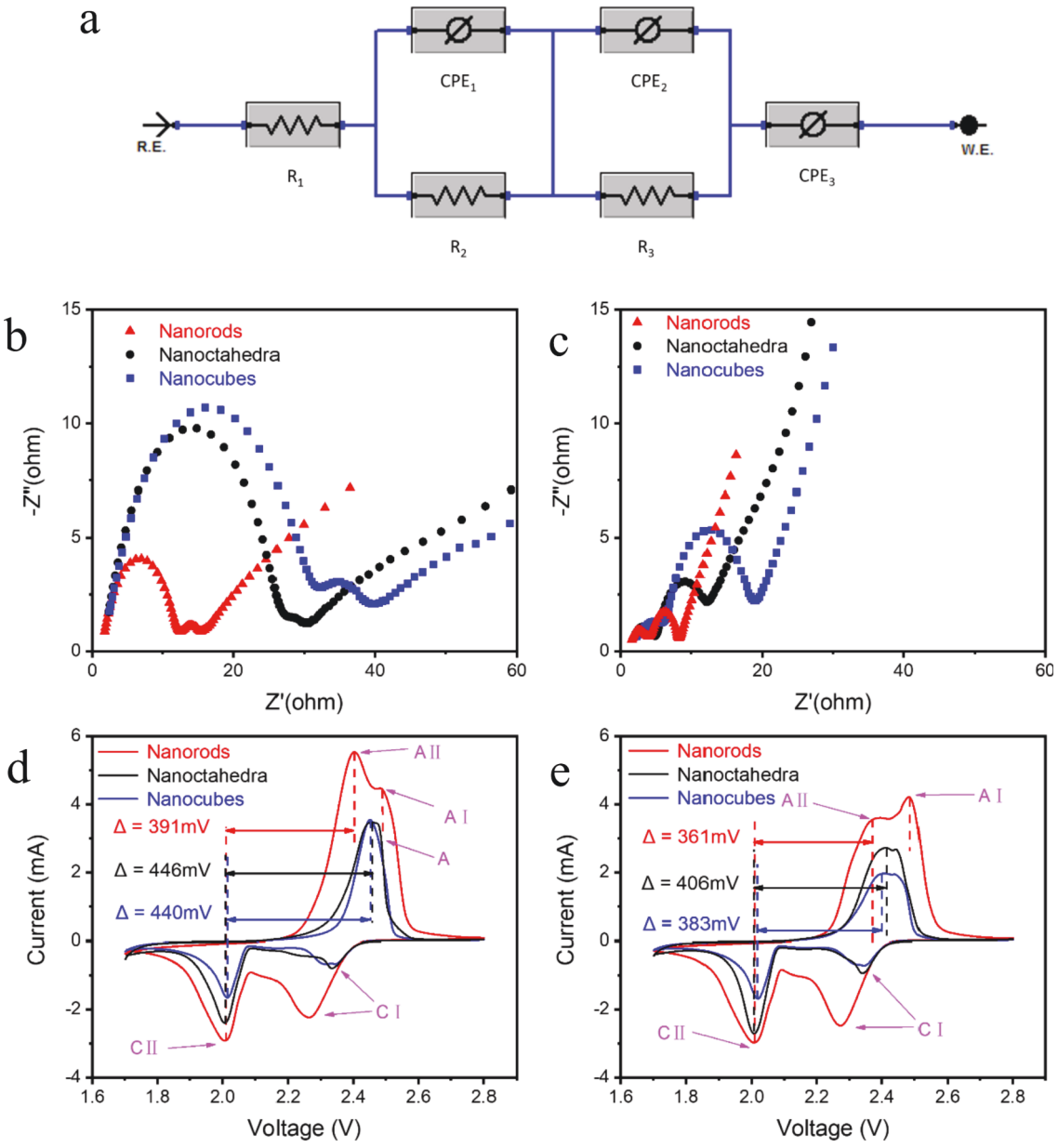

Fig. 3. (a) The equivalent circuit model for EIS curves; (b) EIS curves of CeO_2 NR@CC, CeO_2 NO@CC and CeO_2 NC@CC prior to galvanostatic cycling; (c) EIS curves of CeO_2 NR@CC, CeO_2 NO@CC and CeO_2 NC@CC after 200 galvanostatic cycles at 1C; (d) CV curves of CeO_2 NR@CC, CeO_2 NO@CC and CeO_2 NC@CC for the 1st cycle; (e) CV curves of CeO_2 NR@CC, CeO_2 NO@CC and CeO_2 NC@CC for the 2nd cycle.

lithium polysulfides. This observation can be explained by the strong chemical bonding effect constructed between intermediate polysulfides and CeO_2 NR, leading to favorable inhibition of polysulfide diffusion and excellent cycling performance [44–46].

Cyclic voltammetry (CV) measurement operated within a potential window ranging from 1.7 V to 2.8 V at a scan rate of 0.1 mV s^{-1} was carried out to further understand the underlying mechanisms related to the accelerated electron transport and enhanced redox kinetics of CeO_2 NR@CC compared with the counterparts of CeO_2 NO@CC and CeO_2 NC@CC. For all three assembled coin cells, two representative cathodic peaks (referred as C: C I and C II) can be easily observed from Fig. 3 **d**. The cathodic peak (C I) situated at higher voltage potential (approximately 2.3 V) is attributed to the reductive conversion from elemental sulfur (S8) to soluble long-chain intermediate lithium polysulfide species ($S_8 \rightarrow Li_2S_x$, $x \geq 4$) and the other cathodic peak (C II) located at lower voltage potential (approximately 2.0 V) is associated with the electrochemical reduction from soluble long-chain polysulfide species to insoluble short-chain Li_2S_2/Li_2S ($Li_2S_x \rightarrow Li_2S_2/Li_2S$, $x \geq 4$) [47,48]. It is worth mentioning that the large portion of discharge capacity of rechargeable Li-S battery is realized by the electrochemical reduction from soluble long-chain polysulfide species to insoluble short-chain Li_2S_2/Li_2S at lower potential (the CII region). Therefore, the cathodic peak (C II) located nearby 2.0 V at lower voltage potential plays a more significant role in realizing high discharge capacity of LSBs. All the assembled coin cells manifest a similar position of the cathodic reduction peaks (C II), but the CeO_2 NR@CC electrode cell possesses the largest current response compared with the CeO_2 NO@CC and CeO_2 NC@CC electrode cells. The higher and broader cathodic peak (C II) of the CeO_2 NR@CC electrode with a larger reduction current of 2.93 mA is clearly demonstrated compared to the CeO_2 NO@CC electrode with a reduction current of 2.39 mA (the current of CeO_2 NR@CC is 22.6% higher than that of CeO_2 NO@CC) and the CeO_2 NC@CC electrode with a reduction current of 1.65 mA (the current of CeO_2 NR@CC is 77.6% higher than that of CeO_2 NC@CC), indicating a much stronger electronic and ionic transport capability for the CeO_2 NO@CC electrode cell [49]. In addition, two adjacent anodic peaks (referred as A: A I and A II) can be easily visualized from the CV curve of the CeO_2 NR@CC electrode, representing the electrochemical transformation from insoluble short-chain Li_2S_2/Li_2S to soluble long-chain intermediate lithium polysulfide species ($Li_2S_2/Li_2S \rightarrow Li_2S_x$, $x \geq 4$) and the electrochemical conversion from soluble long-chain intermediate polysulfide species to elemental sulfur ($Li_2S_x \rightarrow S_8$, $x \geq 4$) [50]. However, as depicted in Fig. 3 **d**, only one anodic peak can be seen from the CV curves of the CeO_2 NO@CC electrode and CeO_2 NC@CC electrode, possibly due to: 1) severe polarization issue; 2) slow electronic and ionic transport leading to sluggish redox kinetics; 3) weak chemical interaction with lithium polysulfides resulting in parasitic shuttle effect [51]. All the assembled coin cells have a similar cathodic peak (C II) position, but the anodic peak (A II) of the CeO_2 NR@CC electrode is located at the lowest potential compared with those of the CeO_2 NO@CC electrode and CeO_2 NC@CC electrode. In other worlds, the polarization potential of the CeO_2 NR@CC electrode (391 mV) is smaller than those of the CeO_2 NO@CC electrode (446 mV) and CeO_2 NC@CC (440 mV), indicating a strong chemical affinity between CeO_2 NR and lithium polysulfides [52]. It is also worth mentioning that the higher and broader anodic peak (A II) of the CeO_2 NR@CC electrode with a larger oxidation current of 5.50 mA is clearly observed compared to those of the CeO_2 NO@CC electrode with an oxidation current of 3.46 mA (the current of CeO_2 NR@CC is 59.0% higher than that of CeO_2 NO@CC) and the CeO_2 NC@CC electrode with an oxidation current of 3.52 mA (the current of CeO_2 NR@CC is 56.3% higher than that of CeO_2 NC@CC), demonstrating a significantly enhanced charge transport ability for the CeO_2 NR@CC electrode cell. Fig. 3 **e** exhibits the 2nd scan of the CV curves for CeO_2 NR@CC, CeO_2 NO@CC and CeO_2 NC@CC. These polarization potentials, cathodic peak current (C II), anodic peak current (A II) of CeO_2 NR@CC, CeO_2 NO@CC and CeO_2 NC@CC are summarized in **Table S1**.

Galvanostatic charge discharge cycling ranging from 1.7 V to 2.8 V was performed to gather insights into capacity retention and cycling stability of three button cells with different shaped CeO_2 additives. The 1st galvanostatic cycle profiles of three fabricated coin cells were illustrated in Fig. 4 **a**. In accordance with the CV curves, for all the fabricated electrodes, two representative discharge voltage plateaus can be easily observed from Fig. 4 **a**. The upper discharge plateau situated at higher voltage potential (approximately 2.35 V) is attributed to the reductive conversion from elemental sulfur (S_8) to soluble long-chain intermediate lithium polysulfide species ($S_8 \rightarrow Li_2S_x$, $x \geq 4$) and the lower discharge plateau located at lower voltage potential (approximately 2.05 V) is associated with the electrochemical reduction from soluble long-chain polysulfide species to insoluble short-chain Li_2S_2/Li_2S ($Li_2S_x \rightarrow Li_2S_2/Li_2S$, $x \geq 4$) [53–56]. For the 1st galvanostatic cycle at 0.2C, the discharge capacities of the CeO_2 NR@CC, CeO_2 NO@CC, CeO_2 NC@CC electrodes reached 1261 mAh g^{-1}, 1026 mAh g^{-1} and 810 mAh g^{-1}, respectively. It is worth mentioning that the active material sulfur utilization rate of the CeO_2 NR@CC electrode (75.3%) is higher than those of the CeO_2 NO@CC electrode (61.3%) and CeO_2 NC@CC electrode (48.4%) for the 1st galvanostatic cycle. Additionally, the voltage difference between the charge and discharge plateaus (ΔE) of the CeO_2 NR@CC electrode is smaller than those of the CeO_2 NO@CC electrode and CeO_2 NC@CC electrode, indicating low polarization of the CeO_2 NR@CC electrode compared with the CeO_2 NO@CC electrode and CeO_2 NC@CC electrode, which is in accordance with the CV results. The 100th galvanostatic cycle profiles of three assembled button cells were shown in Fig. 4 **b**. For the 100th galvanostatic cycle at 0.2C, the discharge capacities of the CeO_2 NR@CC, CeO_2 NO@CC, CeO_2 NC@CC electrodes reached 1196 mAh g^{-1}, 995 mAh g^{-1} and 960 mAh g^{-1}, respectively. The active material sulfur utilization rate of the CeO_2 NR@CC electrode (71.4%) is higher than those of the CeO_2 NO@CC electrode (59.4%) and CeO_2 NC@CC electrode (57.3%) for the 100th galvanostatic cycle. The active material sulfur utilization rate can be calculated through the equation shown below.

$$utilization\ rate = \frac{discharge\ capacity}{theoretical\ discharge\ capacity(1675\ mAhg^{-1})} \times 100\%$$

In addition, for the 100th galvanostatic cycle, a smaller polarization of the CeO_2 NR@CC electrode compared with the CeO_2 NO@CC and CeO_2 NC@CC electrodes was also easily observed from Fig. 4 **b**. Capacity retention and cycling reversibility were further investigated by conducting long-term galvanostatic charge discharge cycling for all three fabricated button cells at various current densities (0.2C, 1C and 2C). As depicted in Fig. 4 **c**, it can be seen that the initial discharge capacity of CeO_2 NR@CC was up to 1261 mAh g^{-1} at low current density of 0.2C and approximately 94.8% of the initial discharge capacity was successfully remained after 100 galvanostatic cycles, which results in superior capacity retention with a minimal capacity fading of 0.052% per cycle. Fig. 4 **d** and Fig. 4 **e** exhibited the galvanostatic cycling comparison between three samples at high current density of 1C and 2C, respectively. In order to demonstrate noticeable difference in their galvanostatic cycling performance, **Table S1** summarizes the initial discharge capacity and reversible capacity of three samples at various current densities. The rate performance of the CeO_2 NR@CC, CeO_2 NO@CC and CeO_2 NC@CC electrodes was assessed at different current densities varying from 0.2C to 2C and the corresponding results were exhibited in Fig. 4 **f**. The CeO_2 NR@CC electrode demonstrated favorable discharge capacities of 1195 mAh g^{-1}, 1108 mAh g^{-1}, 1006 mAh g^{-1} and 912 mAh g^{-1} at 0.2C, 0.5C, 1C and 2C, respectively. However, the counterpart CeO_2 NO@CC electrode exhibited low discharge capacities of 1068 mAh g^{-1}, 967 mAh g^{-1}, 870 mAh g^{-1} and 763 mAh g^{-1} at 0.2C, 0.5C, 1C and 2C, respectively. In addition, the counterpart CeO_2 NC@CC electrode manifested low discharge capacities of 977 mAh g^{-1}, 939 mAh g^{-1}, 805 mAh g^{-1} and 583 mAh g^{-1} at 0.2C, 0.5C, 1C and 2C, respectively. It can be concluded that the discharge capacities of the CeO_2 NR@CC electrode at varying current rate were higher than those of

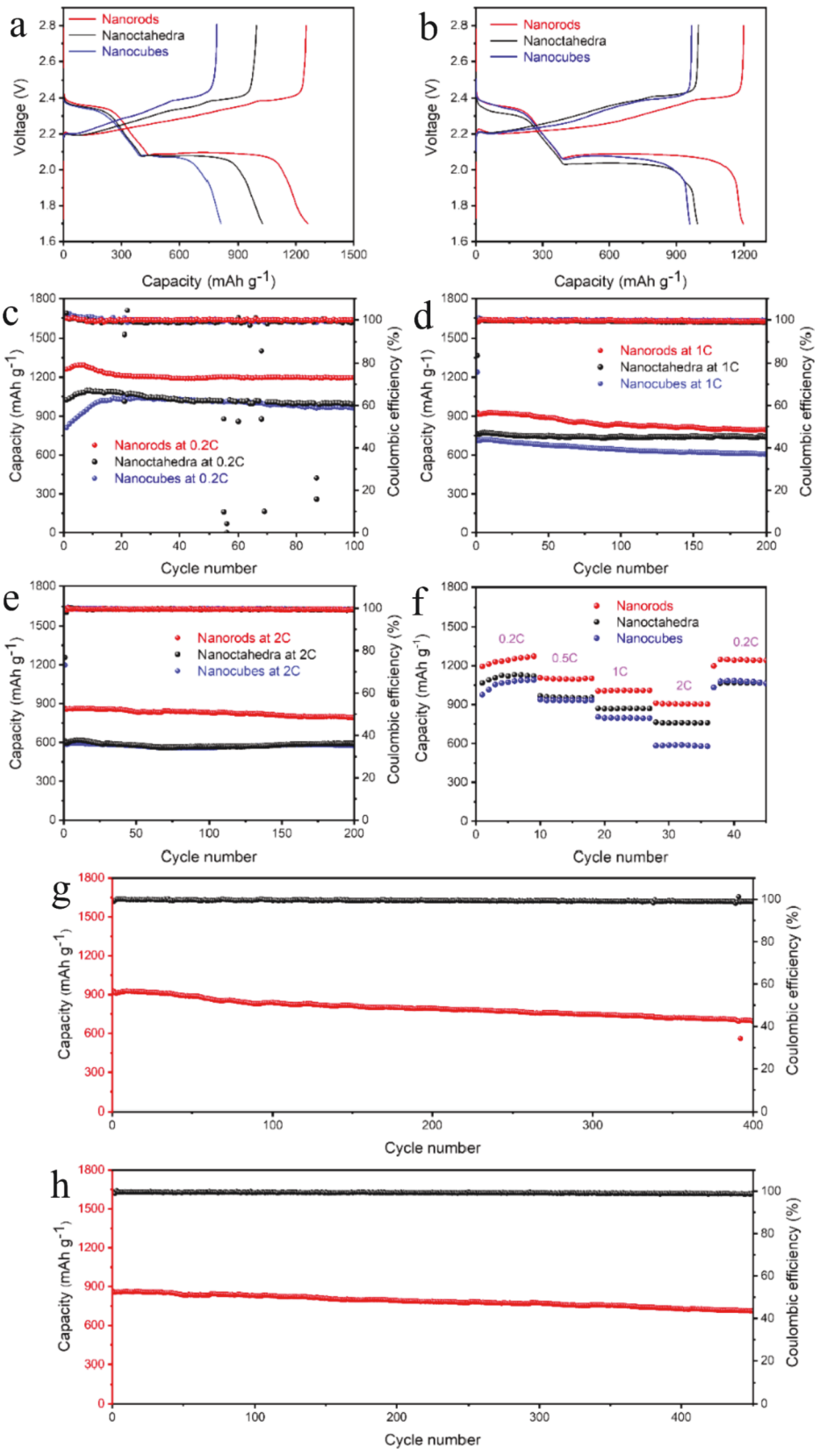

Fig. 4. (a) Galvanostatic charge discharge profiles of CeO_2 NR@CC, CeO_2 NO@CC and CeO_2 NC@CC at 0.2C for (a) the 1st cycle and (b) the 100th cycle; The cycling performance of CeO_2 NR@CC, CeO_2 NO@CC and CeO_2 NC@CC at (c) 0.2C for 100 galvanostatic cycles, (d) 1C for 200 galvanostatic cycles, and (e) 2C for 200 galvanostatic cycles; (f) The comparison of the rate performance of CeO_2 NR@CC, CeO_2 NO@CC and CeO_2 NC@CC electrodes; Long cycle performance of CeO_2 NR@CC: (g) at 1C for 400 cycles and (h) at 2C for 450 cycles.

the CeO_2 NO@CC and CeO_2 NC@CC electrodes. When reverted back to 0.2C, approximately 100% of the initial discharge capacity at 0.2C was remained for the CeO_2 NR@CC electrode. As depicted in Fig. 4 **g**, for the CeO_2 NR@CC electrode, the discharge capacity was well maintained at 697 mAh g^{-1} after 400 galvanostatic cycles at 1C, demonstrating a superior capacity retention with a minimal capacity decay of 0.062% per cycle. As exhibited in Fig. 4 **h**, the CeO_2 NR@CC electrode demonstrated a well-maintained discharge capacity of 712 mAh g^{-1} after 450

galvanostatic cycles at 2C, indicating a superb capacity retention with a minimal capacity attenuation of 0.038% per cycle. As a cathode material of LSBs, the sulfur-loading ability is an indispensable indicator for its performance. Furthermore, taking the practical commercialization into account, the electrochemical measurements for the CeO_2 NR@CC, CeO_2 NO@CC electrode and CeO_2 NC@CC electrodes with high areal sulfur loading (3 mg cm^{-2}) and a smaller amount of electrolyte (40 μL) were carried out (Fig. S4). Two noticeable voltage plateaus still can be easily recognized under high areal sulfur loading of 3 mg cm^{-2} for all three samples (Fig. S4 **a-c**). However, the CeO_2 NR@CC electrode cell displays smaller polarization between the charge curve and the discharge curve. Additionally, the CeO_2 NR@CC electrode cell also demonstrates the highest initial discharge capacity and reversible capacity after 100 cycles at 0.2C (Fig. S4 **d**). The specific values of discharge capacity of three different electrodes with high areal sulfur loading are given in **Table S1**.

3.3. Morphological characterization after cycling

To further understand chemical adsorption capability against polysulfides of three prepared electrodes with different shaped CeO_2, morphological characterization of Li anode surfaces from the disassembled CeO_2 NR@CC, CeO_2 NO@CC and CeO_2 NC@CC coin cells after 200 galvanostatic cycles at 1C was implemented by SEM to gather information about the structural and chemical changes. As demonstrated in Fig. 5 **a-c**, a smooth surface of Li metal anode from the disassembled CeO_2 NR@CC button cell without noticeable pulverization or cracks can be easily seen, providing powerful evidence of lithium polysulfides being efficiently trapped on the cathode side through the strong chemical interaction constructed by CeO_2 NR [57]. In contrast, as depicted in Fig. 5 **d-f and** Fig. 5 **g-i**, the surfaces of Li metal anode from the disassembled CeO_2 NO@CC and CeO_2 NC@CC button cells exhibited numerous cracks, severe pulverization and a large amount of Li_2S_2/Li_2S deposition due to the detrimental side reactions caused by the diffusion of lithium polysulfides between intermediate polysulfide species and Li metal anode [57,58], indicating that the chemical adsorption capability of CeO_2 NO and NC was lower than that of CeO_2 NR. Fig. 6 **a-l** exhibited the corresponding EDS elemental mapping and spectra of the Li anode surfaces from the disassembled CeO_2 NR@CC, CeO_2 NO@CC and CeO_2 NC@CC button cells after 200 galvanostatic cycles at 1C. The surface sulfur concentration of the CeO_2 NR@CC electrode (10.9 wt%) is relatively lower than those of the CeO_2 NO@CC electrode (14.7 wt%) and CeO_2 NC@CC electrode (19.3 wt%), indicating successful immobilization of polysulfides is achieved by CeO_2 NR compared with CeO_2 NO and CeO_2 NC.

Fig. S5 **a-f** displayed the cross-sectional SEM images and EDS line scans of the Li metal anodes from the disassembled CeO_2 NR@CC, CeO_2 NO@CC and CeO_2 NC@CC button cells after 200 galvanostatic cycles at 1C. The EDS line scan of the CeO_2 NR@CC electrode exhibited the minimum thickness of elemental S deposited on the cycled Li anode among three cells indicating the smallest polysulfide penetration and efficient inhibition of polysulfides migration.

3.4. XPS and Raman spectroscopy analysis

The XPS S 2p spectra of the cathodes from the disassembled CeO_2 NR@CC, CeO_2 NO@CC and CeO_2 NC@CC button cells after 200 galvanostatic cycles at 2C were displayed in Fig. 7 **a-c**. The peaks situated at ~ 170.5 eV are assigned to polythionate ($[SO_3S_2SO_3]^{-2}$) and the peaks located at ~ 168.3 eV are attributed to the formation of thiosulfate ($[S_2O_3]^{-2}$) [59–61]. Moreover, the peaks situated at ~ 162.9 eV correspond to the bridged S-S bond (S_B^0) representing the presence of elemental sulfur, and the peaks located at ~ 161.3 eV are attributed to the terminal Li-S bond (S_T^{-1}) indicating the existence of Li_2S_2/Li_2S [62]. For the 200 discharge and charge cycling tests, each galvanostatic cycle started with a discharge process and ended with a charge process. The electrochemical conversion from insoluble Li_2S to elemental sulfur

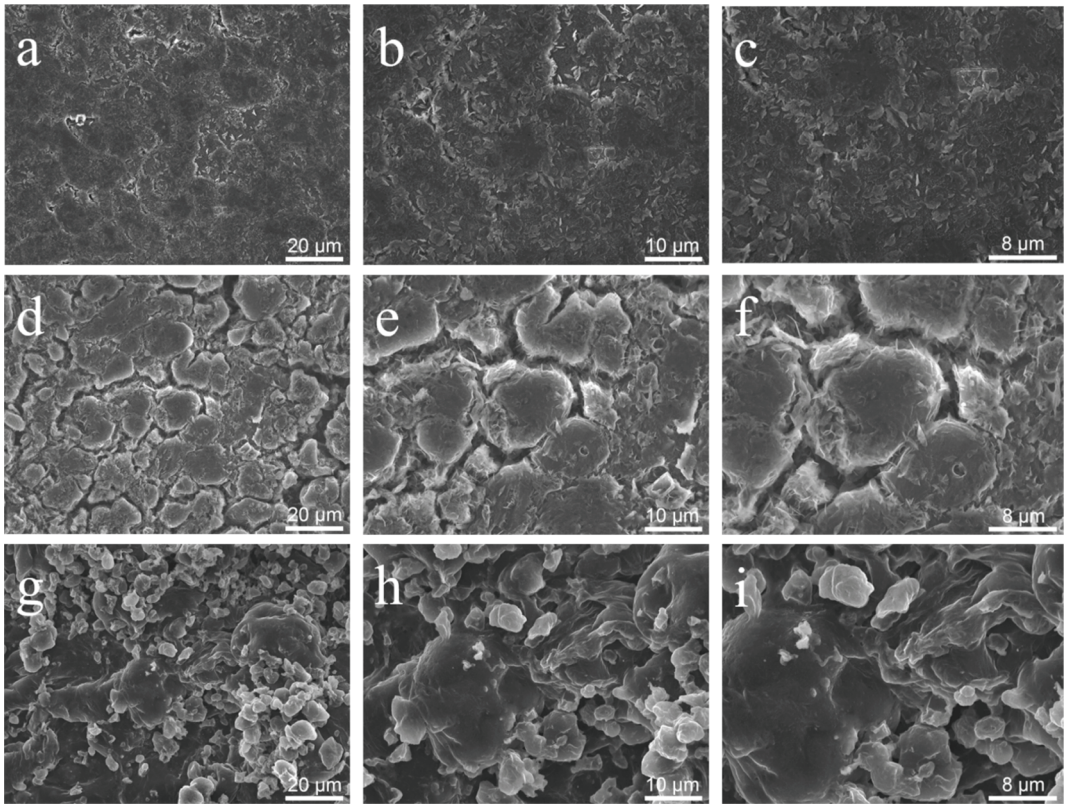

Fig. 5. SEM images of Li anode surface from the disassembled (a-c) CeO_2 NR@CC, (d-f) CeO_2 NO@CC, and (g-i) CeO_2 NC@CC coin cells after 200 galvanostatic cycles at 1C at different magnifications.

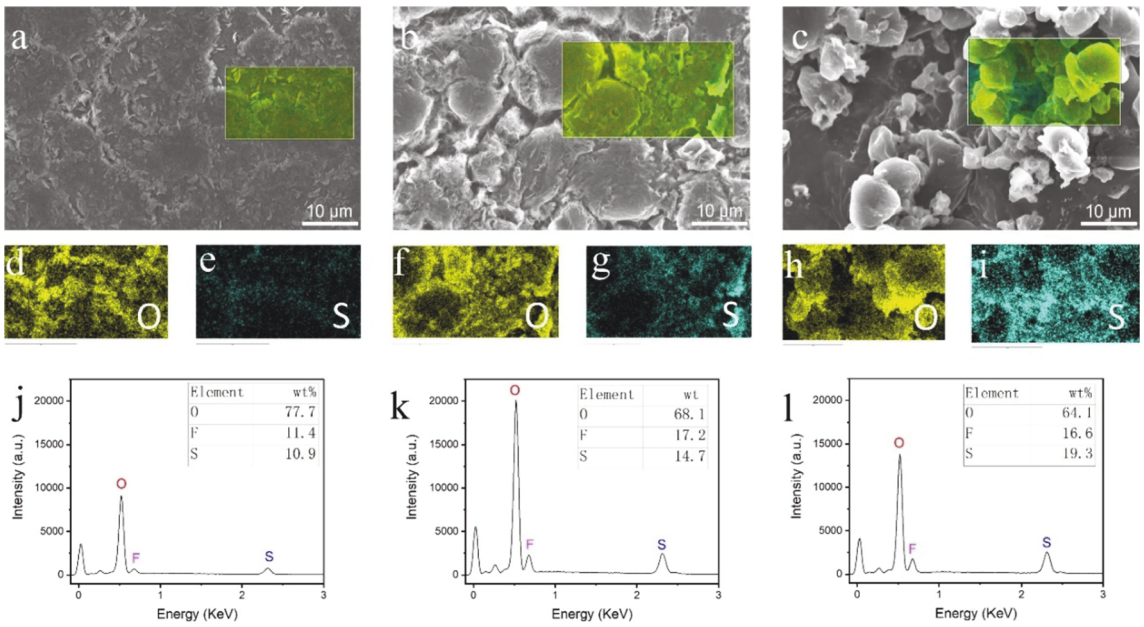

Fig. 6. (a-c) SEM images of the Li anode surfaces from the disassembled CeO_2 NR@CC, CeO_2 NO@CC and CeO_2 NC@CC button cells after 200 galvanostatic cycles at 1C; Corresponding EDS elemental mapping of the Li anode surfaces from the disassembled (d-e) CeO_2 NR@CC, (f-g) CeO_2 NO@CC, and (h-i) CeO_2 NC@CC button cells after 200 galvanostatic cycles at 1C. Corresponding EDS plots of the Li anode surfaces from the disassembled (j) CeO_2 NR@CC, (k) CeO_2 NO@CC, and (l) CeO_2 NC@CC button cells after 200 galvanostatic cycles at 1C.

should be completed when the galvanostatic cycling was finished. The area ratio of elemental sulfur (S_B^0 peaks) to insoluble Li_2S (S_T^{-1} peaks) at the end of the charge process can effectively represents the effectiveness of the electrochemical conversion ($Li_2S \rightarrow Li_2S_x \rightarrow S_8$) of the assembled button cells [62]. In other words, the greater the area ratio of elemental sulfur (S_B^0 peaks) to insoluble Li_2S (S_T^{-1} peaks) is, the better the electrochemical conversion will be. As shown in Fig. 7 **d**, the area ratio of S_B^0 to S_T^{-1} peaks on the surface of the cycled CeO_2 NR@CC cathode (≈4.8) is much greater compared with those of the CeO_2 NO@CC (≈2.8) and CeO_2 NC@CC (≈2.4) cathodes, demonstrating superb electrochemical conversion efficiency of CeO_2 NR@CC. The calculated areas of S_B^0 and S_T^{-1} peaks from the XPS S 2p spectra of three samples are exhibited in **Fig. S6 a-b**. Moreover, the formation of thiosulfate and polythionate is a good indication for an accelerated electrochemical transformation during galvanostatic cycling [63–65]. As displayed in Fig. 7 **e**, the area combination of polythionate and thiosulfate peaks of CeO_2 CC@NR (1151.1 + 110.4≈1261.9) is 14 ~ 20% greater than those of CeO_2 CC@NO (886.9 + 118.9≈1005.8) and CeO_2 CC@NC (1023.5 + 66.7≈1090.2). A possible working mechanism of soluble intermediate polysulfides adsorption via CeO_2 NR is schematically illustrated in Fig. 7 **f**. Firstly, *in-situ* oxidation of polysulfides occurs on the surface of CeO_2 NR with significant amount of surface defects to form the thiosulfate group $[S_2O_3]^{-2}$ with a strong S-O chemical bonding between O of CeO_2 and S of lithium polysulfides [66]. Secondly, thiosulfates $[S_2O_3]^{-2}$ adsorb the newly formed polysulfides to create polythionates $[SO_3S_2SO_3]^{-2}$ and insoluble short-chain Li_2S_2/Li_2S through a disproportionation reaction as shown below [67].

$$[S_2O_3]^{-2} + S_x^{-2} \rightarrow [SO_3S_2SO_3]^{-2} + S_y^{-2} (x \geq 4, y < 3)$$

Moreover, polythionates $[SO_3S_2SO_3]^{-2}$ can function as efficient meditators for accelerating the electrochemical transformation from soluble long-chain polysulfides to insoluble short-chain Li_2S_2/Li_2S as reported previously [68].

Raman spectroscopy was implemented to gain insight of coordination environment and defects (i.e., oxygen vacancies) of three surface engineered CeO_2 additives. As exhibited in **Fig. S7**, the strongest vibrational peak near 460 cm^{-1} corresponds to triply degenerate F_{2g} mode of fluorite structure CeO_2 [69]. For CeO_2 NR, one noticeable band situated near 255 cm^{-1} is attributed to doubly degenerate TO mode (2TA) of CeO_2. Another observable band located near 600 cm^{-1} is assigned to the defect-induced band (D band) used for estimating the concentration of the oxygen vacancy defects [69]. However, these above-mentioned representative 2TA and D defect bands on CeO_2 NR were not observed from the Raman spectra of CeO_2 NC and NO.

3.5. Li_2S_6 adsorption test

Li_2S_6 adsorption test was carried out to gather more information of Li_2S_6 adsorption capability onto CeO_2 NR, NO, NC. As shown in **Fig. S8 a-c**, Li_2S_6 solution containing CeO_2 NR exhibited a noticeable color change after 20 min of the adsorption test and a complete decolorization was fulfilled after 60 min of the test, indicating superior polysulfide adsorption capability. However, the counterparts CeO_2 NC and CeO_2 NO exhibited no apparent color change after 20 min and a slight decolorization after 60 min.

3.6. Possible working mechanism of CeO_2 additive

Based on the previously reported DFT simulation of TiO_2 similarly used as a functional host in LSBs [70–74], we propose a possible working principle of lithium polysulfides adsorption on surface engineered CeO_2 nanocrystals involved in this work as shown in Fig. 8. For the chemical binding mechanism of lithium polysulfides on polar host materials, the surface termination crystal planes and surface defect concentration are keys to immobilize soluble Li_2S_x ($x \geq 4$) and avoid their shuttling to Li anode. To substantiate this hypothesis, CeO_2 nanocrystals with various termination crystal facets (CeO_2 NR with (1 1 0) and (1 0 0) and (1 1 1), CeO_2 NC with (1 0 0) and CeO_2 NO with (1 1 1)) were investigated by comparing the difference in electrochemical performance and understanding the shape-performance correlation.

First of all, the electrochemical measurements and structural characterizations involved in this work showed that CeO_2 NC with preferentially exposed (1 0 0) crystal facets and CeO_2 NO with preferentially exposed (1 1 1) crystal planes were less effective to form strong chemical affinity against polysulfides (i.e., formation of Ce-S and Li-O chemical

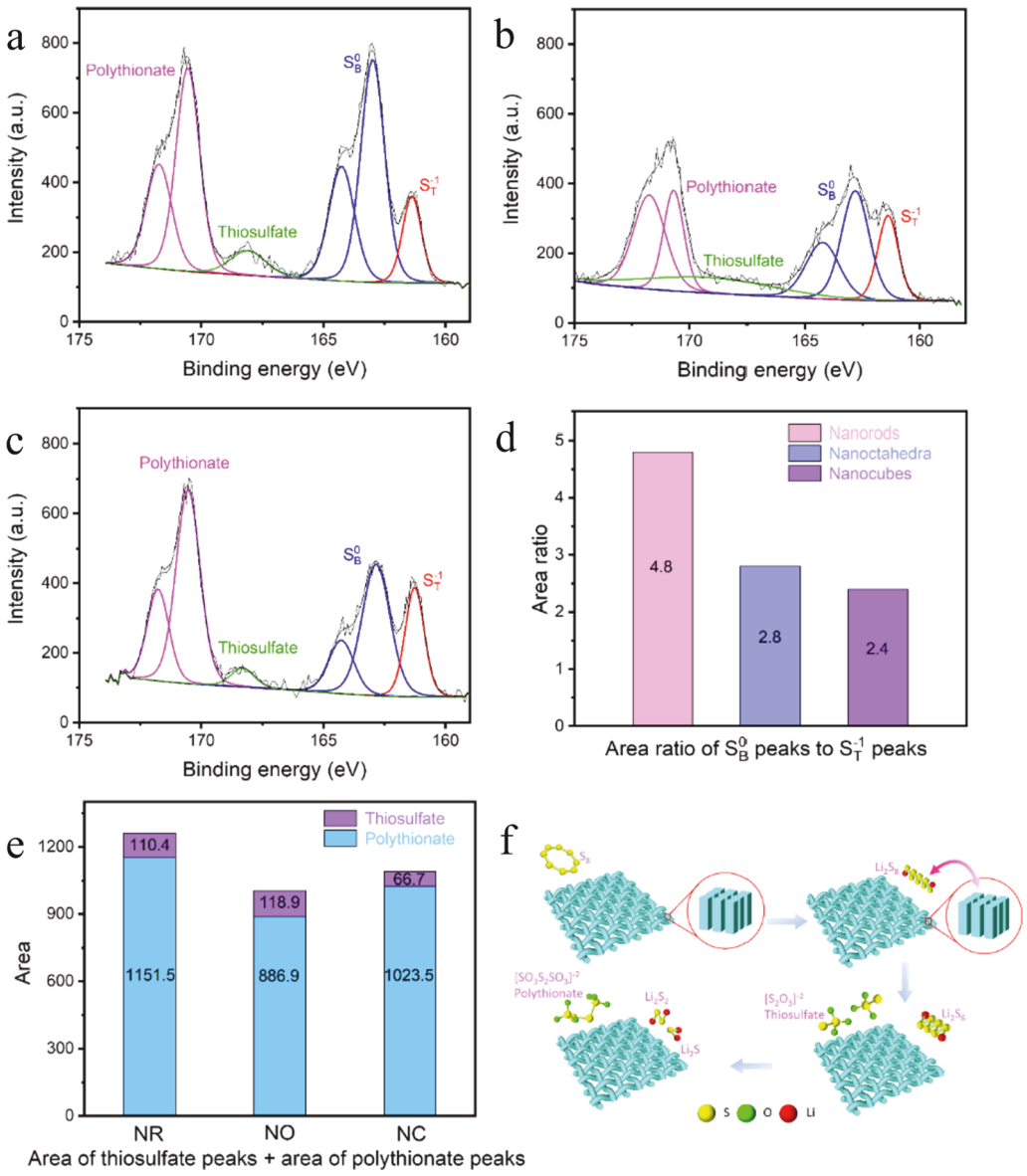

Fig. 7. XPS of S 2p spectra of (a) CeO_2 NR@CC, (b) CeO_2 NO@CC, and (c) CeO_2 NC@CC after 200 galvanostatic cycles at 2C. In the S 2p spectra, the area ratio (d) of S_B^0 peaks to S_T^{-1} peaks for CeO_2 NR@CC, CeO_2 NO@CC and CeO_2 NC@CC. In the S 2p spectra, the integration(e) of the areas of the thiosulfate and polythionate peaks for CeO_2 NR@CC, CeO_2 NO@CC and CeO_2 NC@CC. (f) Schematic diagram of the proposed interaction mechanism of polysulfides and CeO_2 NR@CC.

bonding), resulting in detrimental polysulfides diffusion and poor utilization of sulfur. The CeO_2 NR with preferentially exposed (1 1 0) and (1 0 0) and defected (1 1 1) crystal facets seem to more effectively trap lithium polysulfides and enabling an enhanced electrochemical conversion. Secondly, according to the DFT calculation, polar TiO_2 with different termination planes (110, 101, 100) showed significantly variable binding energies towards Li_2S_4 [70,71,75]. The calculated binding energies of Li_2S_4 on the TiO_2 are − 2.38, −2.41, and − 3.95 eV for plane (1 1 0), plane (1 0 1) and plane (1 0 0), respectively. Therefore, surface engineered CeO_2 with different terminal planes (nanorods with (1 1 0)/(1 0 0)/(1 1 1) planes, nanocubes with (1 0 0) plane and nanoctahedra with (1 1 1) plane) will bind lithium polysulfides differently, which influences their adsorption capability towards polysulfides shuttling. Therefore, surface engineering is an effective approach to controllably obtain CeO_2 nanocrystals with various termination crystal planes and surface defect concentration that can affect the immobilization capability towards intermediate soluble Li_2S_x ($x \geq 4$) and impede their shuttling to Li anode [76,77]. Benefiting from the aforementioned merits, CeO_2 NR are recognized as a more promising candidate of functional sulfur host materials for LSBs.

4. Conclusion

In summary, three CeO_2 NR@CC, CeO_2 NO@CC and CeO_2 NC@CC electrodes were prepared via simple hydrothermal reaction employed as sulfur host materials in LSBs to understand the effects of CeO_2 shape and exposed crystal facets on the adsorption of lithium polysulfides and battery electrochemical performance. Among all three investigated electrodes, the CeO_2 NR@CC electrode exhibited superior capability of immobilizing polysulfides and the best electrochemical performance, which can be attributed to the strong chemical bonding including Ce-S and Li-O bonds formed on the exposed (1 1 0)/(1 0 0) and defected (1 1 1) crystal planes of CeO_2 NR during the electrochemical conversion from long-chain polysulfides to insoluble short-chain Li_2S/Li_2S_2. However, weaker interactions or adsorption of polysulfides was observed on CeO_2 NC and NO with predominant (1 0 0) and (1 1 1) crystal facets, respectively. This study provides new insights into the morphological tailoring for functional sulfur host materials and effective polysulfide

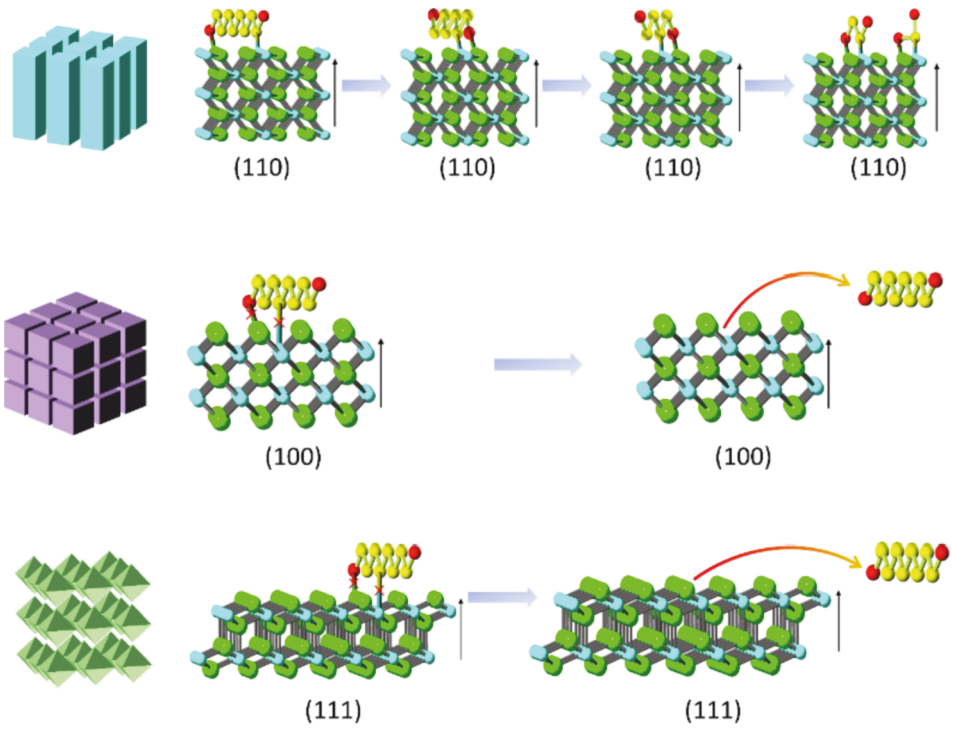

Fig. 8. Schematic illustration of working mechanism of CeO_2 NR, CeO_2 NC and CeO_2 NO against polysulfides.

adsorbents to solve intractable shuttle effect issue and promote high-performance LSBs.

CRediT authorship contribution statement

Zhen Wei: Investigation, Methodology, Formal analysis, Writing – original draft, Writing – review & editing. **Junhao Li:** Formal analysis, Writing – review & editing. **Ruigang Wang:** Conceptualization, Investigation, Methodology, Supervision, Formal analysis, Writing – review & editing, Funding acquisition.

Declaration of Competing Interest

The authors declare that they have no known competing financial interests or personal relationships that could have appeared to influence the work reported in this paper.

Acknowledgement

This work is supported by the National Science Foundation (CBET-2118784 and IIP-2147564). This project also receives partial financial support from Alabama Transportation Institute and Alabama Water Institute. The use of electron microscopy facilities at the Alabama Analytical Research Center (AARC), The University of Alabama, is gratefully acknowledged.

Appendix A. Supplementary material

Supplementary data to this article can be found online at https://doi.org/10.1016/j.apsusc.2021.152237.

References

[1] A. Manthiram, S.H. Chung, C. Zu, Lithium-sulfur batteries: progress and prospects, Adv Mater 27 (2015) 1980–2006.
[2] M. Zhang, W. Chen, L. Xue, Y. Jiao, T. Lei, J. Chu, J. Huang, C. Gong, C. Yan, Y. Yan, Y. Hu, X. Wang, J. Xiong, Adsorption-Catalysis Design in the Lithium-Sulfur Battery, Advanced Energy Materials 10 (2019) 1903008.
[3] J. He, A. Manthiram, A review on the status and challenges of electrocatalysts in lithium-sulfur batteries, Energy Storage Materials 20 (2019) 55–70.
[4] L. Zhang, Y. Wang, Z. Niu, J. Chen, Advanced nanostructured carbon-based materials for rechargeable lithium-sulfur batteries, Carbon 141 (2019) 400–416.
[5] L. Yang, H. Li, Q. Li, Y. Wang, Y. Chen, Z. Wu, Y. Liu, G. Wang, B. Zhong, W. Xiang, Y. Zhong, X. Guo, Research Progress on Improving the Sulfur Conversion Efficiency on the Sulfur Cathode Side in Lithium-Sulfur Batteries, Industrial & Engineering Chemistry Research 59 (2020) 20979–21000.
[6] X. Fang, H. Peng, A revolution in electrodes: recent progress in rechargeable lithium-sulfur batteries, Small 11 (2015) 1488–1511.
[7] L. Chen, L.L. Shaw, Recent advances in lithium–sulfur batteries, Journal of Power Sources 267 (2014) 770–783.
[8] H. Shi, J. Qin, P. Lu, C. Dong, J. He, X. Chou, P. Das, J. Wang, L. Zhang, Z.S. Wu, Interfacial Engineering of Bifunctional Niobium (V)-Based Heterostructure Nanosheet Toward High Efficiency Lean-Electrolyte Lithium-Sulfur Full Batteries, Advanced Functional Materials 31 (2021) 2102314.
[9] B. Chen, T. Wang, S. Zhao, J. Tan, N. Zhao, S.P. Jiang, Q. Zhang, G. Zhou, H. M. Cheng, Efficient Reversible Conversion between MoS2 and Mo/Na2 S Enabled by Graphene-Supported Single Atom Catalysts, Adv Mater 33 (2021), e2007090.
[10] T. Liu, H. Hu, X. Ding, H. Yuan, C. Jin, J. Nai, Y. Liu, Y. Wang, Y. Wan, X. Tao, 12 years roadmap of the sulfur cathode for lithium sulfur batteries (2009–2020), Energy Storage Materials 30 (2020) 346–366.
[11] B. Chen, X. Zhong, G. Zhou, N. Zhao, H.M. Cheng, Graphene-Supported Atomically Dispersed Metals as Bifunctional Catalysts for Next-Generation Batteries Based on Conversion Reactions, Adv Mater (2021), e2105812.
[12] J. Wang, Y. Wu, Z. Shi, C. Wu, Mesoporous carbon with large pore volume and high surface area prepared by a co-assembling route for Lithium-Sulfur Batteries, Electrochimica Acta 144 (2014) 307–314.
[13] J.J. Chen, Q. Zhang, Y.N. Shi, L.L. Qin, Y. Cao, M.S. Zheng, Q.F. Dong, A hierarchical architecture S/MWCNT nanomicrosphere with large pores for lithium sulfur batteries, Phys Chem Chem Phys 14 (2012) 5376–5382.
[14] J. Zhang, Z. Dong, X. Wang, X. Zhao, J. Tu, Q. Su, G. Du, Sulfur nanocrystals anchored graphene composite with highly improved electrochemical performance for lithium–sulfur batteries, Journal of Power Sources 270 (2014) 1–8.
[15] R. Yang, H. Du, Z. Lin, L. Yang, H. Zhu, H. Zhang, Z. Tang, X. Gui, ZnO nanoparticles filled tetrapod-shaped carbon shell for lithium-sulfur batteries, Carbon 141 (2019) 258–265.
[16] L. Fan, H. Wu, X. Wu, M. Wang, J. Cheng, N. Zhang, Y. Feng, K. Sun, Fe-MOF derived jujube pit like Fe3O4/C composite as sulfur host for lithium-sulfur battery, Electrochimica Acta 295 (2019) 444–451.
[17] M. Zhu, S. Li, J. Liu, B. Li, Promoting polysulfide conversion by V2O3 hollow sphere for enhanced lithium-sulfur battery, Applied Surface Science 473 (2019) 1002–1008.
[18] J. Choi, T.-G. Jeong, D. Lee, S.H. Oh, Y. Jung, Y.-T. Kim, Enhanced rate capability due to highly active Ta2O5 catalysts for lithium sulfur batteries, Journal of Power Sources 435 (2019), 226707.

[19] G. Feng, X. Liu, Z. Wu, Y. Chen, Z. Yang, C. Wu, X. Guo, B. Zhong, W. Xiang, J. Li, Enhancing performance of Li–S batteries by coating separator with MnO @ yeast-derived carbon spheres, Journal of Alloys and Compounds 817 (2020), 152723.
[20] L. Ma, R. Chen, G. Zhu, Y. Hu, Y. Wang, T. Chen, J. Liu, Z. Jin, Cerium Oxide Nanocrystal Embedded Bimodal Micromesoporous Nitrogen-Rich Carbon Nanospheres as Effective Sulfur Host for Lithium-Sulfur Batteries, ACS Nano 11 (2017) 7274–7283.
[21] W. Qi, W. Jiang, F. Xu, J. Jia, C. Yang, B. Cao, Improving confinement and redox kinetics of polysufides through hollow NC@CeO2 nanospheres for high-performance lithium-sulfur batteries, Chemical Engineering Journal 382 (2020), 122852.
[22] D. Xiao, C. Lu, C. Chen, S. Yuan, CeO2-webbed carbon nanotubes as a highly efficient sulfur host for lithium-sulfur batteries, Energy Storage Materials 10 (2018) 216–222.
[23] W.-I. Hsiao, Y.-S. Lin, Y.-C. Chen, C.-S. Lee, The effect of the morphology of nanocrystalline CeO2 on ethanol reforming, Chemical Physics Letters 441 (2007) 294–299.
[24] S.T. Hossain, Y. Almesned, K. Zhang, E.T. Zell, D.T. Bernard, S. Balaz, R. Wang, Support structure effect on CO oxidation: A comparative study on SiO2 nanospheres and CeO2 nanorods supported CuOx catalysts, Applied Surface Science 428 (2018) 598–608.
[25] T. Désaunay, G. Bonura, V. Chiodo, S. Freni, J.P. Couzinié, J. Bourgon, A. Ringuedé, F. Labat, C. Adamo, M. Cassir, Surface-dependent oxidation of H 2 on CeO 2 surfaces, Journal of Catalysis 297 (2013) 193–201.
[26] S. Afzal, X. Quan, S. Lu, Catalytic performance and an insight into the mechanism of CeO2 nanocrystals with different exposed facets in catalytic ozonation of p-nitrophenol, Applied Catalysis B: Environmental 248 (2019) 526–537.
[27] X. Zheng, Y. Li, L. Zhang, L. Shen, Y. Xiao, Y. Zhang, C. Au, L. Jiang, Insight into the effect of morphology on catalytic performance of porous CeO2 nanocrystals for H2S selective oxidation, Applied Catalysis B: Environmental 252 (2019) 98–110.
[28] S.-Y. Zhao, S.-P. Wang, Y.-J. Zhao, X.-B. Ma, An in situ infrared study of dimethyl carbonate synthesis from carbon dioxide and methanol over well-shaped CeO 2, Chinese Chemical Letters 28 (2017) 65–69.
[29] W. Chen, R. Ran, D. Weng, X. Wu, J. Zhong, S. Han, Influence of morphology on basicity of CeO 2 and its use in 2-chloroethyl ethyl sulfide degradation, Journal of Rare Earths 35 (2017) 970–976.
[30] C. Li, Y. Sun, I. Djerdj, P. Voepel, C.-C. Sack, T. Weller, R. Ellinghaus, J. Sann, Y. Guo, B.M. Smarsly, H. Over, Shape-Controlled CeO2 Nanoparticles: Stability and Activity in the Catalyzed HCl Oxidation Reaction, ACS Catalysis 7 (2017) 6453–6463.
[31] L. Liu, Z. Yao, Y. Deng, F. Gao, B. Liu, L. Dong, Morphology and Crystal-Plane Effects of Nanoscale Ceria on the Activity of CuO/CeO2 for NO Reduction by CO, ChemCatChem 3 (2011) 978–989.
[32] J. Li, Z. Liu, D.A. Cullen, W. Hu, J. Huang, L. Yao, Z. Peng, P. Liao, R. Wang, Distribution and Valence State of Ru Species on CeO2 Supports: Support Shape Effect and Its Influence on CO Oxidation, ACS Catalysis 9 (2019) 11088–11103.
[33] Y. Ge, P. Chen, W. Zhang, Q. Shan, Y. Fang, N. Chen, Z. Yuan, Y. Zhang, X. Feng, Shape-controlled MnO2 as a sulfur host for high performance lithium–sulfur batteries, New Journal of Chemistry 44 (2020) 11365–11372.
[34] Y. Zhang, S. Yao, R. Zhuang, K. Luan, X. Qian, J. Xiang, X. Shen, T. Li, K. Xiao, S. Qin, Shape-controlled synthesis of Ti4O7 nanostructures under solvothermal-assisted heat treatment and its application in lithium-sulfur batteries, Journal of Alloys and Compounds 729 (2017) 1136–1144.
[35] G. Longoni, R.L. Pena Cabrera, S. Polizzi, M. D'Arienzo, C.M. Mari, Y. Cui, R. Ruffo, Shape-Controlled TiO2 Nanocrystals for Na-Ion Battery Electrodes: The Role of Different Exposed Crystal Facets on the Electrochemical Properties, Nano Lett 17 (2017) 992–1000.
[36] Y. Wang, X. Su, S. Lu, Shape-controlled synthesis of TiO2hollow structures and their application in lithium batteries, J. Mater. Chem. 22 (2012) 1969–1976.
[37] S.T. Hossain, E. Azeeva, K. Zhang, E.T. Zell, D.T. Bernard, S. Balaz, R. Wang, A comparative study of CO oxidation over Cu-O-Ce solid solutions and CuO/CeO2 nanorods catalysts, Applied Surface Science 455 (2018) 132–143.
[38] J. Tu, H. Li, T. Lan, S.-Z. Zeng, J. Zou, Q. Zhang, X. Zeng, Facile synthesis of TiN nanocrystals/graphene hybrid to chemically suppress the shuttle effect for lithium-sulfur batteries, Journal of Alloys and Compounds 822 (2020), 153751.
[39] S. Yao, H. Tang, M. Liu, L. Chen, M. Jing, X. Shen, T. Li, J. Tan, TiO2 nanoparticles incorporation in carbon nanofiber as a multi-functional interlayer toward ultralong cycle-life lithium-sulfur batteries, Journal of Alloys and Compounds 788 (2019) 639–648.
[40] W. Yao, C. Chu, W. Zheng, L. Zhan, Y. Wang, "Pea-pod-like" nitrogen-doped hollow porous carbon cathode hosts decorated with polar titanium dioxide nanocrystals as efficient polysulfide reservoirs for advanced lithium–sulfur batteries, Journal of Materials Chemistry A 6 (2018) 18191–18205.
[41] W. Yao, W. Zheng, K. Han, S. Xiao, Ultrathin double-shell nanotubes of narrow band gap titanium oxide@carbon as efficient polysulfide inhibitors towards advanced lithium–sulfur batteries, Journal of Materials Chemistry A 8 (2020) 19028–19042.
[42] Z. Ye, Y. Jiang, T. Feng, Z. Wang, L. Li, F. Wu, R. Chen, Curbing polysulfide shuttling by synergistic engineering layer composed of supported Sn4P3 nanodots electrocatalyst in lithium-sulfur batteries, Nano Energy 70 (2020), 104532.
[43] Q. Peng, F. Yu, W. Wang, A. Wang, F. Wang, Y. Huang, Ultralight polyethylenimine/porous carbon modified separator as an effective polysulfide-blocking barrier for lithium-sulfur battery, Electrochimica Acta 299 (2019) 749–755.
[44] Z. Zhang, A.H. Shao, D.G. Xiong, J. Yu, N. Koratkar, Z.Y. Yang, Efficient Polysulfide Redox Enabled by Lattice-Distorted Ni3Fe Intermetallic Electrocatalyst-Modified Separator for Lithium-Sulfur Batteries, ACS Appl Mater Interfaces 12 (2020) 19572–19580.
[45] A.H. Shao, Z. Zhang, D.G. Xiong, J. Yu, J.X. Cai, Z.Y. Yang, Facile Synthesis of a "Two-in-One" Sulfur Host Featuring Metallic-Cobalt-Embedded N-Doped Carbon Nanotubes for Efficient Lithium-Sulfur Batteries, ACS Appl Mater Interfaces 12 (2020) 5968–5978.
[46] Z. Wei, J. Li, Y. Wang, R. Wang, High-performance Li-S batteries enabled by polysulfide-infiltrated free-standing 3D carbon cloth with CeO2 nanorods decoration, Electrochimica Acta 388 (2021), 138645.
[47] D. Cai, L. Wang, L. Li, Y. Zhang, J. Li, D. Chen, H. Tu, W. Han, Self-assembled CdS quantum dots in carbon nanotubes: induced polysulfide trapping and redox kinetics enhancement for improved lithium–sulfur battery performance, Journal of Materials Chemistry A 7 (2019) 806–815.
[48] D. Cai, M. Lu, J. Li, D. Cao, H. Chen, J. Tu, W.H. Li, A Highly Conductive MOF of Graphene Analogue Ni3 (HITP)2 as a Sulfur Host for High-Performance Lithium-Sulfur Batteries, Small 15 (2019), e1902605.
[49] Z.L. Xu, S. Lin, N. Onofrio, L. Zhou, F. Shi, W. Lu, K. Kang, Q. Zhang, S.P. Lau, Exceptional catalytic effects of black phosphorus quantum dots in shuttling-free lithium sulfur batteries, Nat Commun 9 (2018) 4164.
[50] C. Wang, H. Song, C. Yu, Z. Ullah, Z. Guan, R. Chu, Y. Zhang, L. Zhao, Q. Li, L. Liu, Iron single-atom catalyst anchored on nitrogen-rich MOF-derived carbon nanocage to accelerate polysulfide redox conversion for lithium sulfur batteries, Journal of Materials Chemistry A 8 (2020) 3421–3430.
[51] D. Tian, X. Song, M. Wang, X. Wu, Y. Qiu, B. Guan, X. Xu, L. Fan, N. Zhang, K. Sun, MoN Supported on Graphene as a Bifunctional Interlayer for Advanced Li-S Batteries, Advanced Energy Materials 9 (2019) 1901940.
[52] M. Chen, X. Zhao, Y. Li, P. Zeng, H. Liu, H. Yu, M. Wu, Z. Li, D. Shao, C. Miao, G. Chen, H. Shu, Y. Pei, X. Wang, Kinetically elevated redox conversion of polysulfides of lithium-sulfur battery using a separator modified with transition metals coordinated g-C3N4 with carbon-conjugated, Chemical Engineering Journal 385 (2020), 123905.
[53] M. Xu, P. Dong, T. Li, H. Hua, Y. Li, X. Li, Y. Zhang, Y. Zhang, J. Zhao, Promoting kinetics of polysulfides redox reactions by the multifunctional CoS/C/CNT microspheres for high-performance lithium-sulfur batteries, Applied Surface Science 504 (2020), 144463.
[54] B. Ye, C. Feng, G. Zhu, S. Wang, A. Fakhri, Feather duster liked CeO2 as efficient adsorber host material for advanced lithium–sulfur batteries, Journal of Alloys and Compounds 823 (2020), 153743.
[55] S. Yan, J. Wu, Y. Dai, Z. Pan, W. Sheng, J. Xu, K. Song, Excellent electrochemical application of Ni-based hydroxide/biomass porous carbon/sulfur composite cathode on lithium-sulfur batteries, Colloids and Surfaces A: Physicochemical and Engineering Aspects 591 (2020), 124513.
[56] Y. Huang, X. Sun, J. Wang, X. Li, W. Chen, C. Wei, H. Hu, G. Liang, Hydroxylated sandwich-structure interlayer as a polysulfide reservoir for lithium-sulfur battery, Journal of Alloys and Compounds 776 (2019) 187–193.
[57] Z. Zhang, S. Basu, P. Zhu, H. Zhang, A. Shao, N. Koratkar, Z. Yang, Highly sulfiphilic Ni-Fe bimetallic oxide nanoparticles anchored on carbon nanotubes enable effective immobilization and conversion of polysulfides for stable lithium-sulfur batteries, Carbon 142 (2019) 32–39.
[58] J. Yan, X. Liu, H. Qi, W. Li, Y. Zhou, M. Yao, B. Li, High-Performance Lithium-Sulfur Batteries with a Cost-Effective Carbon Paper Electrode and High Sulfur-Loading, Chemistry of Materials 27 (2015) 6394–6401.
[59] W. Yao, W. Zheng, J. Xu, C. Tian, K. Han, W. Sun, S. Xiao, ZnS-SnS@NC Heterostructure as Robust Lithiophilicity and Sulfiphilicity Mediator toward High-Rate and Long-Life Lithium-Sulfur Batteries, ACS Nano 15 (2021) 7114–7130.
[60] D.K. Lee, Y. Chae, H. Yun, C.W. Ahn, J.W. Lee, CO2-Oxidized Ti3C2Tx-MXenes Components for Lithium-Sulfur Batteries: Suppressing the Shuttle Phenomenon through Physical and Chemical Adsorption, ACS Nano 14 (2020) 9744–9754.
[61] F. Ma, Y. Wan, X. Wang, X. Wang, J. Liang, Z. Miao, T. Wang, C. Ma, G. Lu, J. Han, Y. Huang, Q. Li, Bifunctional Atomically Dispersed Mo-N2/C Nanosheets Boost Lithium Sulfide Deposition/Decomposition for Stable Lithium-Sulfur Batteries, ACS Nano 14 (2020) 10115–10126.
[62] B. Li, Q. Su, L. Yu, J. Zhang, G. Du, D. Wang, D. Han, M. Zhang, S. Ding, B. Xu, Tuning the Band Structure of MoS2 via Co9S8@MoS2 Core-Shell Structure to Boost Catalytic Activity for Lithium-Sulfur Batteries, ACS Nano 14 (2020) 17285–17294.
[63] X. Ding, R. Gu, P. Shi, Q. Xu, Y. Min, A three-dimensional hierarchical porous carbon network decorated with MnO2 nanoparticles (HPCM) as an efficient sulfur host for high-performance lithium-sulfur batteries (LSBs), Journal of Alloys and Compounds 835 (2020), 155206.
[64] Q. Shao, D. Guo, C. Wang, J. Chen, Yolk-shell structure MnO2@Hollow carbon nanospheres as sulfur host with synergistic encapsulation of polysulfides for improved Li–S batteries, Journal of Alloys and Compounds 842 (2020), 155790.
[65] S. Rehman, T. Tang, Z. Ali, X. Huang, Y. Hou, Integrated Design of MnO2 @Carbon Hollow Nanoboxes to Synergistically Encapsulate Polysulfides for Empowering Lithium Sulfur Batteries, Small 13 (2017) 1700087.
[66] H. Chen, W.-D. Dong, F.-J. Xia, Y.-J. Zhang, M. Yan, J.-P. Song, W. Zou, Y. Liu, Z.-Y. Hu, J. Liu, Y. Li, H.-E. Wang, L.-H. Chen, B.-L. Su, Hollow nitrogen-doped carbon/sulfur@MnO2 nanocomposite with structural and chemical dual-encapsulation for lithium-sulfur battery, Chemical Engineering Journal 381 (2020), 122746.
[67] L. Ni, Z. Wu, G. Zhao, C. Sun, C. Zhou, X. Gong, G. Diao, Core-Shell Structure and Interaction Mechanism of gamma-MnO2 Coated Sulfur for Improved Lithium-Sulfur Batteries, Small 13 (2017) 1603466.
[68] W. Sun, X. Ou, X. Yue, Y. Yang, Z. Wang, D. Rooney, K. Sun, A simply effective double-coating cathode with MnO 2 nanosheets/graphene as functionalized

interlayer for high performance lithium-sulfur batteries, Electrochimica Acta 207 (2016) 198–206.
[69] Z. Liu, J. Li, M. Buettner, R.V. Ranganathan, M. Uddi, R. Wang, Metal-Support Interactions in CeO2- and SiO2-Supported Cobalt Catalysts: Effect of Support Morphology, Reducibility, and Interfacial Configuration, ACS Appl Mater Interfaces 11 (2019) 17035–17049.
[70] M. Cheng, T. Han, M. Zhang, H. Zhang, B. Sun, S. Zhu, M. Zhai, Y. Wu, J. Liu, Hydrogel and sulfur co-coating on semispherical TiO2 as polysulfides-immobilized cathodes for high capacity and stable rate performance lithium-sulfur batteries, Applied Surface Science 513 (2020), 145887.
[71] H.-E. Wang, K. Yin, N. Qin, X. Zhao, F.-J. Xia, Z.-Y. Hu, G. Guo, G. Cao, W. Zhang, Oxygen-deficient titanium dioxide as a functional host for lithium–sulfur batteries, Journal of Materials Chemistry A 7 (2019) 10346–10353.
[72] G. Chen, J. Li, N. Liu, Y. Zhao, J. Tao, G. Kalimuldina, Z. Bakenov, Y. Zhang, Synthesis of nitrogen-doped oxygen-deficient TiO2-x/reduced graphene oxide/sulfur microspheres via spray drying process for lithium-sulfur batteries, Electrochimica Acta 326 (2019), 134968.
[73] C. Zha, D. Wu, T. Zhang, J. Wu, H. Chen, A facile and effective sulfur loading method: Direct drop of liquid Li2S8 on carbon coated TiO2 nanowire arrays as cathode towards commercializing lithium-sulfur battery, Energy Storage Materials 17 (2019) 118–125.
[74] W. Dong, D. Wang, X. Li, Y. Yao, X. Zhao, Z. Wang, H.-E. Wang, Y. Li, L. Chen, D. Qian, B.-L. Su, Bronze TiO2 as a cathode host for lithium-sulfur batteries, Journal of Energy, Chemistry 48 (2020) 259–266.
[75] Y. Yu, M. Yan, W.-D. Dong, L. Wu, Y.-W. Tian, Z. Deng, L.-H. Chen, T. Hasan, Y. Li, B.-L. Su, Optimizing inner voids in yolk-shell TiO2 nanostructure for high-performance and ultralong-life lithium-sulfur batteries, Chemical Engineering Journal 417 (2021), 129241.
[76] J. Li, Z. Liu, R. Wang, Support structure and reduction treatment effects on CO oxidation of SiO2 nanospheres and CeO2 nanorods supported ruthenium catalysts, J Colloid Interface Sci 531 (2018) 204–215.
[77] R. Wang, R. Dangerfield, Seed-mediated synthesis of shape-controlled CeO2nanocrystals, RSC Adv. 4 (2014) 3615–3620.